ACCSCIENCE PUBLISHING

Asian Journal of Water, Environment and Pollution

REVIEW ARTICLE

Morphology engineering of graphitic carbon nitride for enhanced photocatalytic performance: A mini-review

Mingjuan Zhang[1]*, Jingyi Zhao[1], Ziyi Wei[1], Xing Zhang[2], and Qihong Liu[2]*

[1]Anhui Province Engineering Research Center of Water and Soil Resources Comprehensive Utilization and Ecological Protection in High Groundwater Mining Area, Anhui University of Science and Technology, Huainan, China

[2]Hunan Institute of Animal and Veterinary Science, Changsha, China

Abstract

Graphitic carbon nitride (g-C_3N_4) has emerged as a promising visible-light-driven photocatalyst for environmental remediation and energy conversion due to its suitable bandgap, high stability, and low cost. However, bulk g-C_3N_4 prepared by conventional thermal polymerization suffers from low specific surface area, limited active sites, and severe charge recombination. To address these limitations, various morphology engineering strategies have been developed. This review systematically summarizes the preparation methods of g-C_3N_4 with different morphologies, including ultrathin nanosheets via thermal oxidation etching, liquid-phase ultrasonic exfoliation, and chemical exfoliation; mesoporous structures using hard templating; tubular structures through molecular self-assembly; as well as spherical, rod-like, and quantum dot morphologies. These morphological modifications effectively increase the specific surface area, shorten charge migration pathways, and provide more reactive sites, thereby significantly enhancing photocatalytic hydrogen evolution and pollutant degradation. This review aims to offer guidance for designing high-performance g-C_3N_4 photocatalysts.

Keywords: Photocatalysis; Graphitic carbon nitride; Morphology engineering; Ultrathin nanosheets; Mesoporous structures

***Corresponding authors:**
Mingjuan Zhang (mingjuan678@163.com);
Qihong Liu (liuqh@hunaas.cn)

Citation: Zhang M, Zhao J, Wei Z, Zhang X, Liu Q. Morphology engineering of graphitic carbon nitride for enhanced photocatalytic performance: A mini-review. *Asian J Water Environ Pollut.* 2026;23(4):026160105. doi: 10.36922/AJWEP026160105

Received: April 15, 2026

Revised: May 15, 2026

Accepted: May 25, 2026

Published online: June 19, 2026

1. Introduction

Photocatalytic technology, as a green and sustainable approach for environmental remediation and energy conversion, has garnered widespread attention in recent years.[1] Its core principle is based on the energy band structure of semiconductor materials: when the incident light energy is greater than or equal to the semiconductor bandgap (E_g), electrons in the valence band (VB) are excited and transition to the conduction band (CB), leaving behind holes in the VB, thereby forming electron-hole pairs.[2] These photogenerated charge carriers migrate to the material surface, participate in redox reactions, generate reactive oxygen species (ROS), or drive processes, *e.g.*, H_2 evolution and CO_2 reduction.[3,4] The positions of the E_{CB} and E_{VB} of a semiconductor determine its reduction and oxidation capabilities, while parameters, *e.g.*, Fermi level (E_f) and work function (W_s), influence the built-in electric field strength of heterojunctions and the charge carrier separation efficiency.[5]

Among the numerous semiconductor photocatalysts, graphitic carbon nitride (g-C_3N_4) stands out due to its unique advantages.[6] As an organic polymeric semiconductor composed of carbon and nitrogen, g-C_3N_4 features abundant earth reserves, low synthesis cost, and excellent thermal and chemical stability.[7] Its energy band structure enables direct utilization of visible light, and its photogenerated electrons and holes possess high redox potentials, presenting broad application prospects in environmental remediation and energy fields.[8,9] However, bulk g-C_3N_4 prepared by traditional thermal polymerization suffers from low specific surface area, insufficient active sites, and severe photogenerated carrier recombination, which limit its photocatalytic efficiency.[10-12]

To overcome these drawbacks, researchers have developed various morphology control strategies.[13,14] This article systematically reviews the preparation methods of different morphologies of g-C_3N_4 and their effects on photocatalytic performance, including ultrathin nanosheets (via thermal oxidation etching, liquid-phase ultrasonic exfoliation, and chemical exfoliation), mesoporous structures (hard templating), tubular structures (molecular self-assembly), as well as other morphologies, *e.g.*, spherical, rod-like, and quantum dots. By tuning the morphology, one can effectively increase the specific surface area, shorten charge carrier migration pathways, and provide more reactive active sites, thereby significantly enhancing the efficiency of photocatalytic hydrogen production and pollutant degradation. This review aims to provide a reference for the design and development of high-performance g-C_3N_4 photocatalysts.

2. Basic principle of photocatalytic technology

In general, the photocatalysis technology is based on semiconductor, although the precious metals with the surface plasmon resonance (SPR) effect, *e.g.*, gold (Au) and organic molecules have been reported to be available for photocatalytic H_2 production and CO_2 reduction.[15-17] The energy bands of semiconductors (Figure 1) formed by the splitting of energy levels with similar energies are discontinuous, where a E_g consisting of conduction band (CB) and valence band (VB) exists.[18] When a semiconductor absorbs photons with energy equal to or greater than its E_g, electrons are excited from the VB to the CB, leaving holes in the VB. The number of photoexcited electrons equals that of holes, forming electron-hole pairs.[19] The separation of electron-hole pairs formed electrons and holes, which migrated to the surface of semiconductor for participating in the subsequent redox reaction. It should be noted that not all photogenerated carriers reach the surface, recombination can occur in the bulk or at surface defects, which is a key limitation for semiconductor.[20]

The reduction potential of CB and the oxidation potential of VB determine whether electrons can reduce O_2 and holes can oxidize H_2O to ROS.[21,22] For $\cdot O_2^-$ formation: the CB edge potential must be more negative than $O_2/\cdot O_2^-$ (-0.33 eV vs. NHE). For ·OH formation: the VB edge potential must be more positive than $OH^-/\cdot OH$ (2.40 eV vs. NHE) or $H_2O/\cdot OH$ (2.72 eV vs. NHE), the holes on the VB can oxidize OH^- or H_2O to ·OH and H_2O_2. In addition to E_{CB}, E_{VB} and E_g, the energy band structures of semiconductor also include E_f and W_s. The energy level corresponding to E_f has a 1/2 probability of being occupied by electrons, and the W_s is the difference between vacuum energy level (E_{vac}) and E_f.[23] There are three types of semiconductors, i.e., intrinsic, n-type and p-type. The E_f of intrinsic, n-type and p-type semiconductor is located in the middle of E_g, near the E_{CB} and near the E_{VB}, respectively.[24] With regard to the composites composed of semiconductor and metal, metallic compound or other semiconductor, their E_f and W_s affect the strength of the built-in electric field, and thus affect the separation efficiency of electron-hole pairs.

2.1. The semiconductor g-C_3N_4

Recently, the g-C_3N_4 as a crystalline all-organic middle band gap semiconductor has attracted extensive attention in the field of environmental remediation and energy fields.[25] The g-C_3N_4 is mainly composed of two elements, *i.e.*, C and N, which are abundant on the Earth. The organic chemistry nature means that the cost required to prepare g-C_3N_4 is relatively low, and its properties can be simply adjusted without changing the overall composition too much.[26]

2.1.1. Energy band structures of g-C_3N_4

The basic structural units of g-C_3N_4 are triazine and heptazine (tri-s-triazine) rings (Figure 2a and 2b).[27] Density Functional Theory (DFT) calculations showed that the heptazine-based structure is ~30 kJ/mol more stable than the triazine-based one.[28] Experimental evidence confirmed that pyrolysis of cyanamide, dicyandiamide, urea, or melamine yields a melon polymer with heptazine units.[29,30] These units stack along the z-axis via van der Waals forces and possible hydrogen bonding (due to defects and residual H atoms), forming a graphite-like interlayer structure with an interlayer distance (d_s) of ~0.327 nm. Higher thermal condensation temperatures reduce defects and lead to tighter stacking, while nanostructures or porous g-C_3N_4 may exhibit slightly decreased d_s.[31,32]

2.1.2. Structural characteristics of g-C_3N_4

The g-C_3N_4 possesses high thermal and chemical stability.

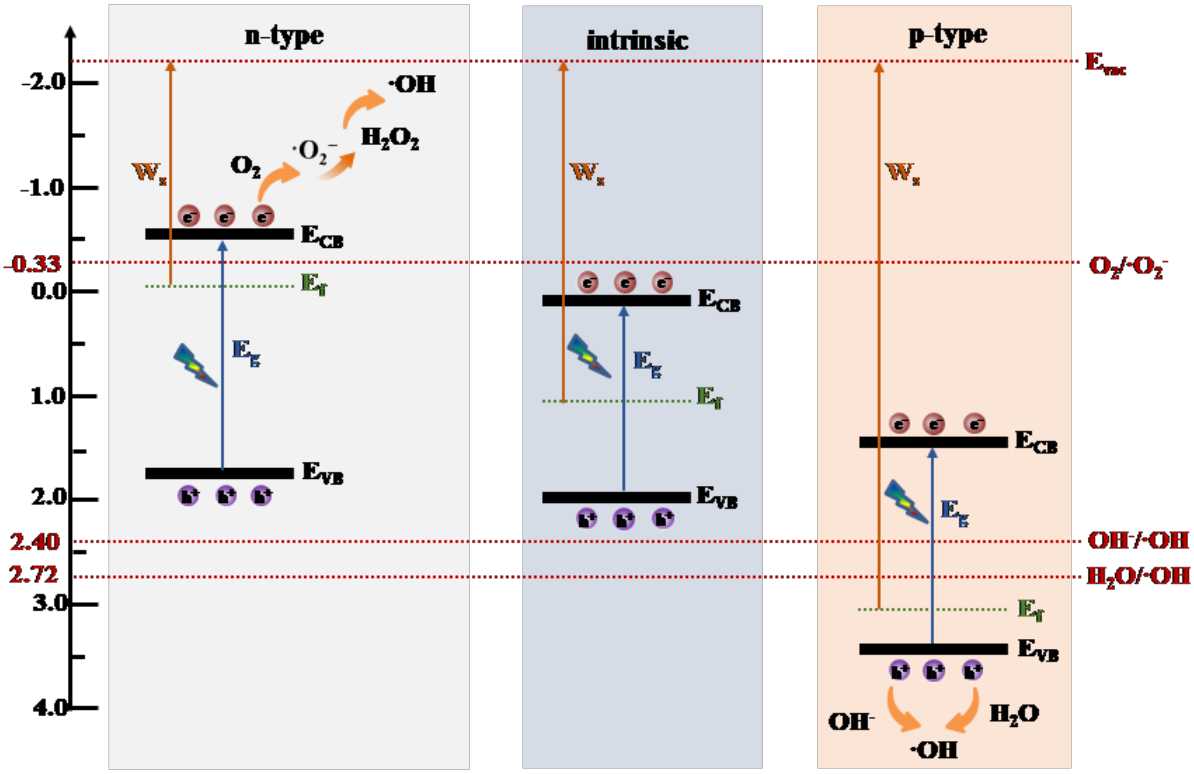

Figure 1. The energy band structure of n-type, intrinsic and p-type semiconductors. We assumed that the $E_{CB} \geq O_2/·O_2^-$ (−0.33 eV vs. NHE) of a n-type semiconductor, and the $E_{VB} \geq OH^-/·OH$ (2.40 eV vs. NHE) and $H_2O/·OH$ (2.72 eV vs. NHE) of a p-type semiconductor.

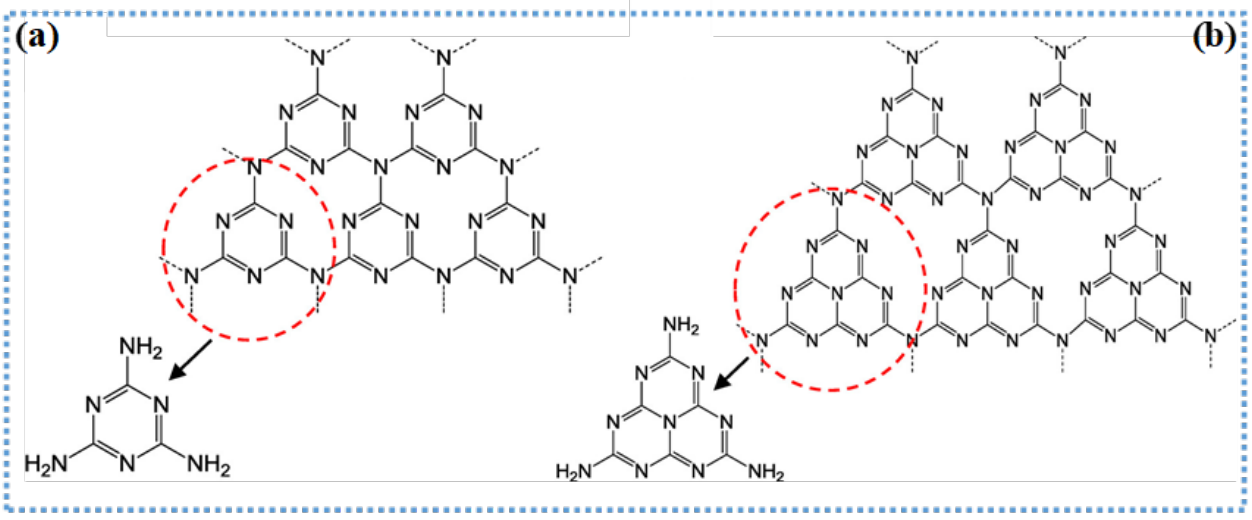

Figure 2. The basic structural units: (a) triazine and (b) tri-s-triazine (heptazine) structures of g-C_3N_4. Both panels are reproduced with permission from Ong *et al.*[27] Copyright © 2016 American Chemical Society.

Thermogravimetric analysis showed no significant volatilization up to 600 °C in air, with decomposition starting at 630 °C.[33,34] It is insoluble in most solvents (water, acetone, ethanol, N,N-dimethylformamide [DMF], dilute NaOH, *etc.*); Fourier transform infrared spectroscopy (FT-IR) spectra remain unchanged after 30 days of soaking.[35,36] As a mid-bandgap semiconductor, g-C_3N_4 exhibits E_g = 2.7 eV, E_{CB} = −1.1 eV and E_{VB} = +1.6 eV, enabling direct visible-light utilization and high redox potentials.[37] It was not until 2006 that Goettmann *et al.*[38] first adopted g-C_3N_4 as a non-metallic catalyst to activate benzene, avoiding the use of metal chlorides and halogenated compounds. In 2009, Wang *et al.*[39] manifested that g-C_3N_4 could decompose water into H_2 under visible light irradiation in the presence of sacrificial donor. However, bulk g-C_3N_4 prepared by direct thermal polymerization has small specific surface area (SB_{ET}) (<10 m^2 g^{-1}), limited active sites, and severe electron-hole recombination due to long interlayer migration paths and strong Coulomb interactions.[40-42]

3. Preparation methods of g-C_3N_4 with different morphologies

In recent years, researchers have employed a variety of methods to prepare the g-C_3N_4 with a specific morphology, *e.g.*, the ultrathin g-C_3N_4 nanosheets[43], the monatomic layer mesoporous g-C_3N_4 nanonets[44], the g-C_3N_4 quantum dots[45], the ball g-C_3N_4[46], and hollow tubular g-C_3N_4[47] for improving the photocatalytic performance of monomer bulk g-C_3N_4.

3.1.1. Thermal oxidation etching method

The thermal oxidation etching is a simple top-down strategy, which has the advantages of low cost, easy scale and environmental friendliness. The preparation process is as follows[48]: The calcination of as-synthesized bulk g-C_3N_4 is conducted in a muffle furnace (500~550 °C). If the stability of the van der Waals force or hydrogen bonding in the interlayers of bulk g-C_3N_4 is not enough to resist the high temperature oxidation process in muffle furnace, the outer layers and the bare inner layers of the bulk g-C_3N_4 would gradually peel off. With the process of oxidation, the thickness of the bulk g-C_3N_4 decreased continuously and the ultrathin g-C_3N_4 nanosheets are generated. The ultrathin g-C_3N_4 nanosheets with a thickness of ~2 nm was successfully prepared by the thermal oxidation etching method. The large SB_{ET} (306 m^2 g^{-1}) of the ultrathin g-C_3N_4 nanosheets could provide abundant reactive sites. In addition, the ultrathin thickness could shorten the path length of electrons and holes from the interior to the surface, reducing the probability of their recombination. Furthermore, the larger E_g (E_g = 2.97 eV) of the ultrathin g-C_3N_4 nanosheets, indicating the redox potential of electrons and holes are stronger as compared to bulk g-C_3N_4. Therefore, the ultrathin g-C_3N_4 nanosheets showed higher photocatalytic performance in producing ·OH and H_2 than that of the bulk g-C_3N_4. It cannot be ignored that the reaction conditions, such as heating rate, calcination temperature, and holding time, should be reasonably controlled during the thermal oxidation etching process to avoid the insufficient reaction produce g-C_3N_4 with a large thickness or the reaction is too intense, the bulk g-C_3N_4 completely oxidized without product formation.

3.1.2. Liquid phase ultrasonic stripping method

The liquid phase ultrasonic stripping is usually conducted by dispersing the bulk g-C_3N_4 in various solvents, such as isopropyl alcohol (IPA), N-methylpyrrolidone (NMP), water, ethanol, and acetone. Subsequently, the dispersion solution was ultrasonic-treated at room temperature.[49] By controlling the ultrasonic time and selecting an instrument with the appropriate power, the bulk g-C_3N_4 was gradually stripped to the ultrathin g-C_3N_4 nanosheets.[50] By using this method, the layered material is stripped into nanosheets through the interaction of solvent molecules, which is affected by the surface energy of the solvent. If the surface energy of the bulk g-C_3N_4 matches that of the solvent, the bulk g-C_3N_4 can be stripped into nanosheets and the enthalpy of the mixture (ΔH_{mix}) is the minimum.[51] Zhang *et al.*[52] reported that the relationship between ΔH_{mix} and the surface energy is shown in the following formula:

$$\frac{\Delta H_{mix}}{V_{mix}} = \frac{2}{T_{bulk}} \left(\delta_G - \delta_{sol}\right)^2 \varnothing \quad (1)$$

where δ_G and δ_{sol} are respectively the square root of g-C_3N_4 and solvent' surface energy, T_{bulk} represents the average thickness of bulk g-C_3N_4, and $\varnothing$ is the volume proportion of g-C_3N_4. They calculated the surface energy of g-C_3N_4 is ~115 mJ m^{-2} by using the DFT calculations, which matched that of water (at ~102 mJ m^{-2}) very well. The results demonstrated that water has the excellent dispersion ability for the stripping of bulk g-C_3N_4. Meanwhile, they prepared the ultrathin g-C_3N_4 nanosheets with a thickness of ~2.5 nm for the first time by the liquid phase ultrasonic stripping method using water as the dispersion solution. Coleman *et al.*[53] showed that the optimal surface energy of solvent were 30 mJ m^{-2} larger than that of the van der Waals bonding surface (70 mJ m^{-2}). The surface energies of IPA and NMP are ~40 mJ m^{-2}, which indicated that both of them can be used as the dispersion solution for the stripping of bulk g-C_3N_4. It was reported that the ultrathin g-C_3N_4 nanosheets with a thickness of ~2 nm and the high S_{BET} was successfully prepared by using IPA as the dispersion

solution.[54] The ultrathin thickness and high S_{BET} not only provided more reactive sites, but facilitated the separation and migration of electrons and holes. The as-prepared g-C_3N_4 nanosheets exhibited average H_2 production rate of 93 μmol h^{-1} under visible light irradiation.

Besides, Han *et al.*[55] synthesized the ultrathin g-C_3N_4 nanosheets with monatomic layer by adopting freeze-dried self-assembled dicyandiamide as a precursor, water and IPA as solvents. Due to the unique structural advantages in energy level arrangement, electrons and holes transfer, light absorption and reaction sites, the monatomic layer mesoporous g-C_3N_4 nanonets prepared by the liquid phase ultrasonic stripping method have the excellent photocatalytic H_2 evolution performance. The photocatalytic H_2 production rate is as high as 8510 μmol h^{-1} g^{-1} and the apparent quantum efficiency is 5.1% under visible light irradiation (λ > 420 nm), which is the highest among the reported g-C_3N_4 nanosheets. It manifested that the liquid phase ultrasonic stripping method is simple, mild, environmentally friendly (solvent recyclable) and is capable of preparing the high-quality 2D materials on a large scale.

The ultrathin g-C_3N_4 nanosheets prepared by the thermal oxidation etching and liquid phase ultrasonic stripping method revealed the higher photocatalytic H_2 evolution and organic pollutants degradation performance as compared to the direct thermal polymerization process prepared bulk g-C_3N_4.[56-58] The theoretical thickness of the monatomic layer g-C_3N_4 is 0.327 nm, meaning that these ultrathin g-C_3N_4 nanosheets with a thickness of 2~3 nm contain 6~9 monatomic layers.[59] It can then be expected that the ultrathin g-C_3N_4 nanosheets with fewer atomic layers might have the higher photocatalytic performance. The two-step method, involving liquid-phase ultrasonic stripping in water as a solvent followed by thermal oxidation etching, produced ultrathin g-C_3N_4 nanosheets with a thickness of approximately 1 nm (ca. three atomic layers), which showed efficient photocatalytic H_2 production performance.[60]

3.1.3. Chemical stripping method

The chemical stripping is another frequently-used method for the preparation of the ultrathin g-C_3N_4 nanosheets.[61] Xu *et al.*[62] prepared the monatomic layer ultrathin g-C_3N_4 nanosheets by the chemical stripping method for the first time. Specifically, 1 g bulk g-C_3N_4 was mixed with 10 mL of concentrated H_2SO_4 (98 wt%) in a 50 mL flask at room temperature for 8 h. Then, the mixture was slowly poured into a beaker filled with 100 mL of water for ultrasonic stripping. The resulting suspension was centrifuged at a rate of 3000 rpm/min for 10 min to separate the large particles of g-C_3N_4. The monatomic layer ultrathin g-C_3N_4 nanosheets was obtained by further centrifugation and water washing the luminous yellow suspension to remove the residual H_2SO_4 and drying in an oven at 80 °C for 12 h. The ultrathin g-C_3N_4 nanosheets with a thickness of 0.4 nm have great advantages over the bulk g-C_3N_4 in the separation of electrons and holes, the intensity of photocurrent, the photocatalytic H_2 generation and organic pollutants degradation performance.

3.2. Preparation of mesoporous g-C_3N_4

The hard template method is able to prepare the ordered mesoporous g-C_3N_4 with the high S_{BET}, small particle size, adjustable pore size and controllable morphology by replicating the uniform pore template structure.[63]

3.2.1. Hard template 2D mesoporous silica nanoparticles

Two-dimensional (2D) mesoporous silica nanoparticles, such as SBA-15 and IBN-4, are hard templates that are commonly adopted for the preparation of mesoporous g-C_3N_4.[64] Vinu *et al.*[65] successfully prepared the 2D hexagonal ordered mesoporous g-C_3N_4 with the adjustable S_{BET}, pore size and pore volume for the first time through a simple polymerization reaction of the precursor carbon tetrachloride and ethylenediamine using SBA-15 with the different pore sizes as the hard template. However, the mesoporous g-C_3N_4 prepared with SBA-15 has the low nitrogen content and large particle size due to the poor thermal stability. Subsequently, Jin *et al.*[66] adopted the ultrafine mesoporous silica nanoparticles (IBN-4) as a hard template to prepare mesoporous g-C_3N_4 with a particle size less than 150 nm and the high nitrogen content. It is worth noting that the presence of air in the silica template pore greatly hinders the diffusion of organic precursor of g-C_3N_4 synthesis, completely obstructing penetration of the precursor into the silica template pore. Moreover, water or other solvents contained in the raw material might compete with the absorption of precursor on the template. Therefore, the synthesized mesoporous g-C_3N_4 has a certain degree of structural defects or volume collapse after the removal of template.

In view of that, Zhang *et al.*[67] proposed an optimized synthesis method aimed at effectively removing the previously trapped air from the template to accelerate the diffusion of organic precursors and avoid competitive solvent-induced absorption. Specifically, the SBA-15 was first acidified with 1 M dilute HCL to enhance the surface reactivity on cyanamide containing amido through acid-base interaction. Then, the air in the SBA-15 channel was removed by a technology combining ultrasonic

and vacuum that utilizes relatively low saturated vapor pressure of liquid cyanamide. Besides, the cyanamide was simultaneously pumped into the SBA-15 channel via the bubble collapse effect. Accordingly, the precursor cyanamide could permeate into the SBA-15 channel completely. The g-C_3N_4 prepared with SBA-15 as the hard template using this optimization method has a 2D mesoporous hexagonal skeleton, a larger S_{BET}, and a higher photocatalytic H_2 production performance.

3.2.2. Hard template 3D cage mesoporous silica nanoparticles

It should not be ignored that due to the inherent porous structure limitations of the hard template 2D mesoporous silica nanoparticles, the mesoporous g-C_3N_4 prepared have a pore size of <6 nm and a pore volume of <1.2 $cm^3 g^{-1}$. In order to further optimize the structure of mesoporous g-C_3N_4, the 3D cage mesoporous silica nanoparticles, *e.g.*, SBA-X (X = 1, 2, 6, 12, 16), FDU-X (X = 1, 2, 5, 12), and KIT-X (X = 5, 6), were employed as the hard templates.[68] For example, Lakhi *et al.*[69] prepared the 3D cage mesoporous g-C_3N_4 for the first time by directly polymerizing the precursor carbon tetrachloride and ethylenediamine in the FDU-12 template pore with different pore sizes. In addition, the 3D cage mesoporous g-C_3N_4 prepared with SBA-16 and KIT-6 as the hard template has also been reported.[70] Not only the mesoporous but spherical and rod-shaped g-C_3N_4 can be prepared by the hard template method.[71] Although great progress has been made in the preparation of g-C_3N_4 with the novel layered micro-nanostructures by the hard template method, the removal of template requires etching with the toxic chemicals ammonium difluoride (NH_4HF_2) or hydrogen fluoride (HF), which not only affects the environment and experimental operators but also prevents the further functionalization of g-C_3N_4.[72] Therefore, it is ideal and challenging to prepare g-C_3N_4 with the specific morphology by the template free method.

3.3. Preparation of tubular g-C_3N_4

Ring-shaped organic channel structure (ROCS) linked by 1:1 multiple hydrogen bonding between melamine and cyanuric acid (trithiocyanic acid) created by Rao *et al.*[73] by means of hydrothermal synthesis in 1999 (Figure 3a and 3b) has been widely adopted as the starting material for the preparation of tubular g-C_3N_4. For example, the ordered hollow g-C_3N_4 tube was prepared using the ROCS linked between melamine and cyanuric acid as the starting material.[74] In addition, fish scale tubular g-C_3N_4 was prepared using the ROCS linked between melamine and trithiocyanic acid as the starting material.[75] The molecular self-assembly method to prepare tubular g-C_3N_4 using the ROCS linked between melamine and cyanuric acid (trithiocyanic acid) as the starting material can be divided into three steps, as follows[47]:

(1) the formation of ROCS;
(2) the ROCS form the rod-like supermolecular precursors through the π-π stacking interactions;
(3) the rod-like supermolecular precursors was placed in a tubular furnace with protective gas for the calcination (500–550 °C).

The pyrolysis starts from the center of the rod-like supermolecular precursors and diffused outward to generate tubular g-C_3N_4.[76] The molecular self-assembly method can also be used to prepare the spherical and rod-like g-C_3N_4 through the regulation of solvent and the intermolecular force.[77] The tubular g-C_3N_4 prepared by the molecular self-assembly method has the advantages of orderly structure, large S_{BET}, abundant reaction sites, high separation efficiency of electrons and holes, strong light absorption ability, and superb photocatalytic performance compared with bulk g-C_3N_4.

3.4. Preparation of other morphologies g-C_3N_4

Other morphologies of g-C_3N_4 include spherical, rod-like, and quantum dot. For example, the mesoporous hollow spherical g-C_3N_4 was prepared by the molecular self-assembly method using the ROCS linked between melamine and cyanuric acid as the starting material. The porous spherical g-C_3N_4 was prepared using the spherical mesoporous silica foam and melamine as the hard template and precursors, respectively.[78] It was reported that the g-C_3N_4 nanorods were prepared by the thermal polycondensation method using cyanamide as precursors with eutectic mixture of LiCl-KCl.[79]

Furthermore, the morphologic transformation of g-C_3N_4 from nanoplates to nanorods was realized by a simple reflux method.[80] The formation of g-C_3N_4 nanorods was attributed to the possible peel off and regrowth of nanoplates during the reflux process as well as the edging mechanism of layered structure. As presented in Figure 4a, the g-C_3N_4 quantum dots (CNQDs) was prepared by the multiple stripping steps with bulk g-C_3N_4 as the starting material.[81] Specifically, the bulk g-C_3N_4 was firstly stripped into nanosheets by the thermal oxidation etching method. Then, the g-C_3N_4 nanosheets were further stripped into nanoribbons by the chemical stripping method using the mixed solution of concentrated H_2SO_4 and HNO_3 as solvent. Finally, the g-C_3N_4 quantum dots with diameter distribution of smaller than 5 nm were successfully prepared by the shearing of nanoribbons using the two-step method of liquid phase stripping and hydrothermal (Figure 4b and 4c). The prepared g-C_3N_4 quantum dots with a diameter less than 10 nm have the upconversion

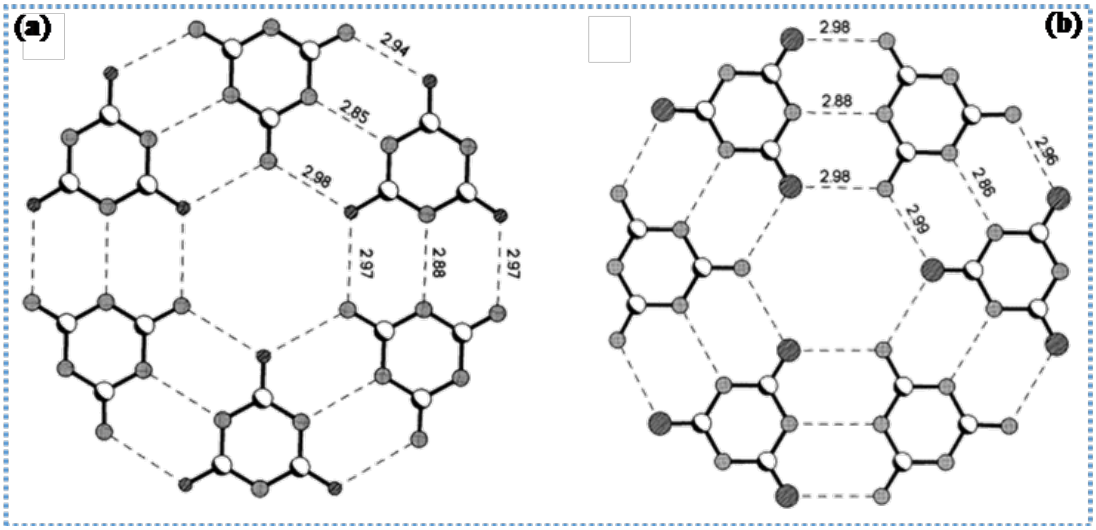

Figure 3. The ring organic channel structure of melamine-cyanuric acid (a) and melamine-trithiocyanuric acid (b). Both panels are reproduced with permission from Ranganathan and Rao.[73] Copyright © 1999 Wiley.

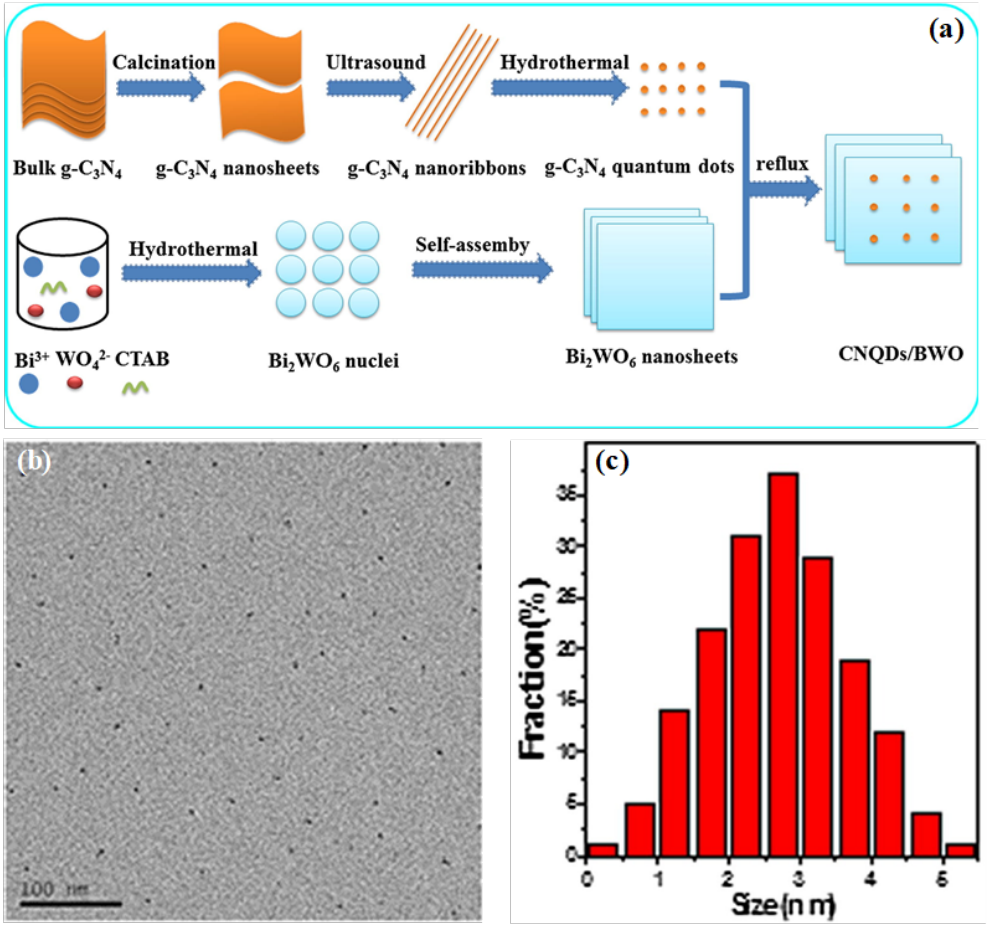

Figure 4. The preparation process, morphology, and size distribution of CNQDs. (a) The schematic diagram illustrating the synthesis of CNQDs/BWO composites. (b) The g-C_3N_4 quantum dots. (c) The diameter distribution of the CNQDs. Reproduced with permission from Zhang *et al.*[81] Copyright © 2019 Elsevier.

effect and are able to convert the near-infrared (NIR) light into visible (Vis) light for the degradation of organic dyes.

The preparation methods of different g-C_3N_4 and their influences on photocatalytic performance are summarized in Table 1. It can be seen that ultrathin nanosheets achieve high photocatalytic H_2 production and ·OH generation activity by widening the E_g and shortening the carrier migration path. Their preparation method is simple but the yield is relatively low, and the ultrasonic exfoliation method has moderate scalability. Mesoporous structures significantly enhance the efficiency of active site and charge separation due to ordered channels and high S_{BET}. However, the removal of hard templates requires the use of toxic reagents, which is costly and limited in scale. The tubular structure enhances light absorption and electron-hole separation through one-dimensional charge transport and multiple light scattering. It does not require a template but needs precise control of self-assembly conditions, and has moderate scalability. Although spherical/rod-shaped structures can increase the S_{BET} and shorten the diffusion path, the hard template method has the problem of toxic etching, and the reflux method has a limited yield and low scalability. Quantum dots have a wide E_g, upconversion luminescence and abundant edge sites, which can achieve a wide spectral response. However, their preparation steps are numerous and the yield is low. Currently, they are only suitable for laboratory-scale applications. Overall, different morphology engineering strategies each offer distinct advantages in enhancing photocatalytic performance, but the greenness, controllability and large-scale potential of their preparation processes still need further improvement.

4. Conclusion and outlooks

The photocatalytic performance is closely related to the morphology of semiconductors. This review clarifies the common strategies for preparing g-C_3N_4 with different morphologies and explains the improvement in photocatalytic performance from the perspectives of light absorption and charge transport. Morphology engineering is further elaborated in the following:

(1) Morphology engineering is an effective strategy to enhance the photocatalytic performance of g-C_3N_4. Converting bulk g-C_3N_4 into different morphologies, such as ultrathin nanosheets, mesoporous structures, and tubular structures, can significantly increase the specific surface area, shorten the migration path of photogenerated charge carriers, and provide more active sites, thereby effectively suppressing electron-

Table 1. Comparison of different morphology engineering strategies of g-C_3N_4

Morphology	Band structure/Charge behavior	Photocatalytic performance	Advantages/Limitations/Scalability
Ultrathin nanosheets	Broadened bandgap; shortened charge carriers migration path	High H_2 evolution; enhanced •OH production	*Advantages:* Simple; high activity *Limitations:* Low yield *Scalability:* Moderate ultrasonic exfoliation scalable
Mesoporous structures	Enhanced active sites; improved charge carriers separation	High H_2 evolution; effective pollutant degradation	*Advantages:* Ordered porosity; tunable pore size; high S_{BET} *Limitations:* Toxic template remova; limited scalability *Scalability:* Low-hazardous etching; template synthesis costly
Tubular structures	1D charge transport along tube walls; strong light absorption due to multiple scattering; efficient electron-hole separation	Superior H_2 evolution; enhanced visible light activity	*Advantages:* Template-free; ordered structure; high activity *Limitations:* Requires precise control of self-assembly conditions; batch-to-batch variation *Scalability:* Moderate-supramolecular synthesis relatively simple, but calcination step energy-intensive
Spherical/ rod-like	Increased S_{BET}; shortened charge carriers diffusion pathways	Efficient degradation of organic dyes; high H_2 evolution	*Advantages:* Diverse morphologies *Limitations:* Hard templating requires toxic etching; reflux method yields limited quantity *Scalability:* Low to moderate dependence on method
Quantum dots	Broadened bandgap; upconversion converts near-infrared (NIR) to visible light; abundant edge sites	Efficient photocatalytic degradation of organic pollutants under wide spectrum light	*Advantages:* Unique optical properties; excellent for photosensitization *Limitations:* Multi-step process; low yield; difficult to scale *Scalability:* Low, currently limited to lab scale only

hole recombination and improving photocatalytic efficiency.

(2) Various morphology adjustment methods have their own advantages: thermal oxidation etching and liquid-phase ultrasonic exfoliation are suitable for preparing ultrathin nanosheets; hard templating is effective for constructing ordered mesoporous structures; and molecular self-assembly excels in producing special morphologies, such as tubular and spherical structures. Among these, liquid-phase ultrasonic exfoliation is more promising for green synthesis due to its mild conditions and recyclable solvents.

(3) Morphology modification also contributes to optimized energy band structure and reaction activity. Ultrathin nanosheets and quantum dots not only increase the specific surface area but also broaden the bandgap and enhance the redox capability. For instance, single-atom-layer mesoporous g-C_3N_4 nanonets exhibit a photocatalytic hydrogen evolution rate as high as 8510 μmol $h^{-1}g^{-1}$, far superior to conventional bulk materials.

Although significant progress has been made in optimizing the photocatalytic performance of g-C_3N_4, further work is required to enhance its practical applicability.

(1) Green and controllable template-free synthesis: Current hard templating methods require toxic reagents (HF or NH_4HF_2) for template removal. Future efforts should focus on template self-sacrifice, vapor deposition, or supramolecular self-assembly to achieve precise morphology control and environmental friendliness.

(2) Coupling morphology engineering with heterojunction/defect engineering: Morphology modification alone provides limited charge separation improvement. Integrating Z-scheme or S-scheme heterojunctions, elemental doping, and defect engineering into hierarchical morphologies (*e.g.*, nanosheets grown on tubes, mesoporous spheres loaded with quantum dots) can synergistically boost performance.

(3) Scalable production: While liquid-phase ultrasonic exfoliation and molecular self-assembly showed moderate scalability, the yield of ultrathin nanosheets and quantum dots remained low. Developing continuous-flow or energy-efficient processes is urgently needed.

(4) *In situ* characterization and structure-activity relationships: Real-time tracking of charge carrier dynamics and surface active sites using *in situ* X-ray photoelectron spectroscopy (XPS), transient absorption spectroscopy, and *in situ* FT-IR, combined with DFT calculations, is essential to reveal the mechanistic roles of specific morphologies and guide rational design.

(5) Expanding application scenarios: Beyond H_2 evolution and pollutant degradation, morphology-optimized g-C_3N_4 should be explored for CO_2 reduction, N_2 fixation, photothermal catalysis, and self-cleaning surfaces.

(6) Data-driven analysis and systematic assessment: Beyond traditional qualitative reviews, emerging bibliometric and meta-analytic approaches have been successfully applied to analyze research trends and quantitatively assess the environmental effects of nanomaterials.[82,83] Future studies on g-C_3N_4 morphology engineering could adopt such data-driven strategies to identify knowledge gaps, evaluate conflicting results, and guide the rational design of high-performance photocatalysts.

Acknowledgments

None.

Funding

This work was supported by the Scientific Research Foundation for High-level Talents of Anhui University of Science and Technology (2023yjrc121), Anhui Province Engineering Research Center of Water and Soil Resources Comprehensive Utilization and Ecological Protection in High Groundwater Mining Area (2024-WSREPMA-06).

Conflict of interest

The authors declare that they have no known competing financial interests or personal relationships that could have appeared to influence the work reported in this paper.

Author contributions

Conceptualization: Mingjuan Zhang
Funding acquisition: Mingjuan Zhang
Project administration: Jingyi Zhao, Qihong Liu
Supervision: Jingyi Zhao, Ziyi Wei, Xing Zhang, Qihong Liu
Writing–original draft: Mingjuan Zhang
Writing–review & editing: Jingyi Zhao, Ziyi Wei, Xing Zhang, Qihong Liu

Availability of data

Not applicable.

References

1. Ma D, Xue Q, Liu Y, *et al.* Manipulating interfacial charge

redistribution in $Mn_{0.5}Cd_{0.5}S$/N-rich C_3N_5 S-scheme heterojunction for high-performance photocatalytic removal of emerging contaminants. *J Mater Sci Technol*. 2026;243:265-274.

doi: 10.1016/j.jmst.2025.05.011

2. Wang Q, Zhou Q, Wang P, *et al.* S-scheme POM/MIL-101(Fe) heterojunction for photocatalytic decontamination of Cr(VI). *Sep Purif Technol*. 2025;361:131498.

doi: 10.1016/j.seppur.2025.131498

3. Li S, Wang X, Xue B, *et al.* Flower-like $Ag/Ag_2O/Bi_{12}O_{17}Cl_2$ heterojunction for photocatalytic removal of antibiotics: Synergetic effect of plasmonic effect and p–n heterojunction. *J Mater Sci Technol*. 2026;246:237-246.

doi: 10.1016/j.jmst.2024.12.088

4. Feng C, Wu ZP, Huang KW, *et al.* Surface Modification of 2D Photocatalysts for Solar Energy Conversion. *Adv Mater*. 2022;34:e2200180.

doi: 10.1002/adma.202200180

5. Qi B, Shen R, Ren Z, *et al.* Bifunctional S-scheme sp^2-carbon COF/CdS heterojunction for efficient photocatalytic H_2 evolution and C–C coupling of 5-hydroxymethylfurfural. *J Mater Sci Technol*. 2025;232:65-73.

doi: 10.1016/j.jmst.2025.03.003

6. You C, Zhang X, Zhao Y, *et al.* Plasmonic effect augmented S-scheme mechanism in $Ag/Ag_2O/C_3N_5$ photocatalyst enables efficient photocatalytic degradation of antibiotics. *J Mater Sci Technol*. 2026;242:64-74.

doi: 10.1016/j.jmst.2025.05.002

7. Lazaar N, Wu S, Qin S, *et al.* Single-Atom Catalysts on C_3N_4: Minimizing Single Atom Pt Loading for Maximized Photocatalytic Hydrogen Production Efficiency. *Angew Chem Int Ed Engl*. 2025;64:e202416453.

doi: 10.1002/anie.202416453

8. Etafo NO, Bamisaye A, Bamidele MO, *et al.* Beyond the Swipe: A Review of Photocatalytic Antimicrobial Biocompatible Touchscreen Technology. *Appl Mater Today*. 2025;44:102697.

doi: 10.1016/j.apmt.2025.102697

9. Feng C, Raziq F, Hu M, *et al.* Photoexcitation Altered Reaction Pathway Greatly Facilitate Ammonia Synthesis Over Isolated Ru Sites. *Adv Energy Mater*. 2024;14:2303792.

doi: 10.1002/aenm.202303792

10. Wang Z, Ding G, Huang H, *et al.* Unraveling the dipole field in ultrathin, porous, and defective carbon nitride nanosheets for record-high piezo-photocatalytic H_2O_2 production. *eScience*. 2025;5:100370.

doi: 10.1016/j.esci.2024.100370

11. Zhou X, Zhou Y, Zhao S, *et al.* Precise Mo-Fe Dual-Atom Coordination Regulates the Selective Generation of Non-Free Radicals in Peroxymoncosulfate Activation. *Adv Funct Mater*. 2025;36:e13232.

doi: 10.1002/adfm.202513232

12. Feng C, Tang L, Deng Y, *et al.* Synthesis of Leaf-Vein-Like g-C_3N_4 with Tunable Band Structures and Charge Transfer Properties for Selective Photocatalytic H_2O_2 Evolution. *Adv Funct Mater*. 2020;30:2001922.

doi: 10.1002/adfm.202001922

13. Liu X, Chen S, Tantai X, *et al.* Regulating defects in sulfur-doped $Bi_4O_5I_2$ and constructing S-scheme heterojunctions with g-C_3N_4 to enhance photocatalytic antibiotic degradation. *Sep Purif Technol*. 2025;363:132001.

doi: 10.1016/j.seppur.2025.132001

14. Guo Y, Feng H, Zhang L, *et al.* Insights into the Mechanism of Selective Removal of Heavy Metal Ions by the Pulsed/Direct Current Electrochemical Method. *Environ Sci Technol*. 2024;58:5589-5597.

doi: 10.1021/acs.est.3c10553

15. Jaiswal S, Giri A, Mandal D, *et al.* UV-to-NIR Harvesting Conjugated Porous Polymer Nanocomposite: Upconversion and Plasmon Expedited Thioether Photooxidation. *Angew Chem Int Ed Engl*. 2023;62:e202312910.

doi: 10.1002/anie.202312910

16. Oh Y, Hu XJCSR. Organic molecules as mediators and catalysts for photocatalytic and electrocatalytic CO_2 reduction. *Environ Soc Technol*. 2013;42:2253-2261.

doi: 10.1039/C2CS35276A

17. Lan C, Feng H, Zhang L, *et al.* Regulating electrode wettability by construction of the liquid-liquid interface for improving metal electrodeposition performance. *Chem Eng J*. 2026;527:171769.

doi: 10.1016/j.cej.2025.171769

18. Moon HS, Hsiao KC, Wu MC, *et al.* Spatial Separation of Cocatalysts on Z-Scheme Organic/Inorganic Heterostructure Hollow Spheres for Enhanced Photocatalytic H_2 Evolution and In-Depth Analysis of the Charge-Transfer Mechanism. *Adv Mater*. 2023;35:e2200172.

doi: 10.1002/adma.202200172

19. Liu J, Li S, Qiu Z, *et al.* Stratified Oxygen Vacancies Enhance the Performance of Mesoporous TiO_2 Electron Transport Layer in Printable Perovskite Solar Cells. *Small*. 2023;19:e2300737.

doi: 10.1002/smll.202300737

20. Zhang M, Zhang Y, Zhu Y, *et al.* Insights into adsorption and high photocatalytic oxidation of ciprofloxacin under visible light by intra-molecular Donor-Acceptor like p-n isotype heterojunction: Performance and mechanism. *Chem Eng J*. 2023;464:142533.

doi: 10.1016/j.cej.2023.142533

21. Khan I, Liu W, Zada A, *et al.* Recent progress in emerging materials and hybrid nanocomposites for peroxymonosulfate and peroxydisulfate activation towards solar light-driven photocatalytic degradation of emerging pollutants. *Coord Chem Rev.* 2024;499:215466.

doi: 10.1016/j.ccr.2023.215466

22. Zhou S, Jiang L, Wang H, *et al.* Oxygen Vacancies Modified TiO_2/O-Terminated Ti_3C_2 Composites: Unravelling the Dual Effects between Oxygen Vacancy and High-Work-Function Titanium Carbide. *Adv Funct Mater*. 2023;33:2307702.

doi: 10.1002/adfm.202307702

23. Tan M, Ma Y, Yu C, *et al.* Boosting Photocatalytic Hydrogen Production via Interfacial Engineering on 2D Ultrathin Z-Scheme $ZnIn_2S_4$/g-C_3N_4 Heterojunction. *Adv Funct Mater*. 2022;32:2111740.

doi: 10.1002/adfm.202111740

24. Zhou C, Wang S, Zhao Z, *et al.* A Facet-Dependent Schottky-Junction Electron Shuttle in a $BiVO_4${010}-Au-Cu_2O Z-Scheme Photocatalyst for Efficient Charge Separation. *Adv Funct Mater*. 2018;28:1801214.

doi: 10.1002/adfm.201801214

25. Wang Y, Qu Y, Qu B, *et al.* Construction of Six-Oxygen-Coordinated Single Ni Sites on g-C_3N_4 with Boron-Oxo Species for Photocatalytic Water-Activation-Induced CO_2 Reduction. *Adv Mater*. 2021;33:e2105482.

doi: 10.1002/adma.202105482

26. Hu Y, Zhang S, Zhang Z, *et al.* Enhancing Photocatalytic-Transfer Semi-Hydrogenation of Alkynes Over Pd/C_3N_4 Through Dual Regulation of Nitrogen Defects and the Mott-Schottky Effect. *Adv Mater*. 2023;35:e2304130.

doi: 10.1002/adma.202304130

27. Ong WJ, Tan LL, Ng YH, *et al.* Graphitic Carbon Nitride (g-C_3N_4)-Based Photocatalysts for Artificial Photosynthesis and Environmental Remediation: Are We a Step Closer To Achieving Sustainability? *Chem Rev* 2016;116:7159-7329.

doi: 10.1021/acs.chemrev.6b00075

28. Kroke E, Schwarz M, Horath-Bordon E, *et al.* Tri-s-triazine derivatives. Part I. From trichloro-tri-s-triazine to graphitic C_3N_4 structures. *New J Chem*. 2002;26:508-512.

doi: 10.1039/b111062b

29. Jing L, Xu Y, Xie M, *et al.* Cyano-Rich g-C_3N_4 in Photochemistry: Design, Applications, and Prospects. *Small*. 2024;20:e2304404.

doi: 10.1002/smll.202304404

30. Wang X, Tang W, Jiang L, *et al.* Mechanism insights into visible light-induced crystalline carbon nitride activating periodate for highly efficient ciprofloxacin removal. *Chem Eng J*. 2023;471:144521.

doi: 10.1016/j.cej.2023.144521

31. Merschjann C, Tschierlei S, Tyborski T, *et al.* Complementing Graphenes: 1D Interplanar Charge Transport in Polymeric Graphitic Carbon Nitrides. *Adv Mater*. 2015;27:7993-7999.

doi: 10.1002/adma.201503448

32. Lotsch BV, Doblinger M, Sehnert J, *et al.* Unmasking melon by a complementary approach employing electron diffraction, solid-state NMR spectroscopy, and theoretical calculations-structural characterization of a carbon nitride polymer. *Chemistry*. 2007;13:4969-4980.

doi: 10.1002/chem.200601759

33. Gillan EG. Synthesis of nitrogen-rich carbon nitride networks from an energetic molecular azide precursor. *Chem Mater*. 2000;12(12):3906-3912.

doi: 10.1021/cm000570y

34. Lu H, Zou F, Liu X, *et al.* Z-scheme g-C_3N_4/α-FOD heterojunction-assisted persulfate activation for degradation of tetracycline hydrochloride under visible light: Insights into mechanism. *Chem Eng J*. 2024;479:147224.

doi: 10.1016/j.cej.2023.147224

35. Wang Y, Wang X, Antonietti M. Polymeric graphitic carbon nitride as a heterogeneous organocatalyst: from photochemistry to multipurpose catalysis to sustainable chemistry. *Angew Chem Int Ed Engl*. 2012;51:68-89.

doi: 10.1002/anie.201101182

36. Ren X, Mao M, Feng M, *et al.* Fate, abundance and ecological risks of microcystins in aquatic environment: The implication of microplastics. *Water Res*. 2024;251:121121.

doi: 10.1016/j.watres.2024.121121

37. Zhang Q, Liu X, Chaker M, *et al.* Advancing Graphitic Carbon Nitride-Based Photocatalysts toward Broadband Solar Energy Harvesting. *ACS Mater Lett.* 2021;3:663-697.

doi: 10.1021/acsmaterialslett.1c00160

38. Goettmann F, Fischer A, Antonietti M, *et al.* Metal-free catalysis of sustainable Friedel-Crafts reactions: direct activation of benzene by carbon nitrides to avoid the use of metal chlorides and halogenated compounds. *Chem Commun*. 2006;4530-4532.

doi: 10.1039/b608532f

39. Wang X, Maeda K, Thomas A, *et al.* A metal-free polymeric photocatalyst for hydrogen production from water under visible light. *Nat Mater.* 2009;8:76-80.

doi: 10.1038/nmat2317

40. Teixeira IF, Barbosa ECM, Tsang SCE, *et al.* Carbon nitrides and metal nanoparticles: from controlled synthesis to design principles for improved photocatalysis. *Chem Soc Rev*. 2018;47:7783-7817.

doi: 10.1039/c8cs00479j

41. Zhang M, Tang L, Duan A, *et al.* Adjusting charge kinetics of conjugated polymers via integration of LSPR effect with homojunction. *Chem Eng J*. 2023;452:139068.

doi: 10.1016/j.cej.2022.139068

42. Deng A, Sun Y, Gao Z, *et al.* Internal electric field in carbon nitride-based heterojunctions for photocatalysis. *Nano Energy*. 2023;108:108228.

doi: 10.1016/j.nanoen.2023.108228

43. Liu T, Zeng Y, Ma T, *et al.* Oxygen-Doped Porous Ultrathin Graphitic Carbon Nitride Nanosheets for Photocatalytic Hydrogen Evolution and Rhodamine B Degradation. *Chempluschem*. 2025;90:e202400474.

doi: 10.1002/cplu.202400474

44. Wang Y, Liu L, Ma T, *et al.* 2D Graphitic Carbon Nitride for Energy Conversion and Storage. *Adv Funct Mater*. 2021;31:2102540.

doi: 10.1002/adfm.202102540

45. Qiao Y, Lu H, Wang X, *et al.* Dual S-Scheme Charge Transfer Pathway in g-C_3N_4 Quantum Dots/HKUST-1/TiO_2 Ternary Heterojunctions for Photocatalytic Pollutant Degradation. *Inorg Chem*. 2025;64:21212-21226.

doi: 10.1021/acs.inorgchem.5c03972

46. Dong Z, Yang T, ullah I, *et al.* The influence of morphological changes on the physicochemical and optical properties of g-C_3N_4. *Ceram Int*. 2024;50:17882-17889.

doi: 10.1016/j.ceramint.2024.02.276

47. Guo S, Deng Z, Li M, *et al.* Phosphorus-Doped Carbon Nitride Tubes with a Layered Micro-nanostructure for Enhanced Visible-Light Photocatalytic Hydrogen Evolution. *Angew Chem Int Ed Engl*. 2016;55:1830-1834.

doi: 10.1002/anie.201508505

48. Niu P, Zhang L, Liu G, *et al.* Graphene-Like Carbon Nitride Nanosheets for Improved Photocatalytic Activities. *Adv Funct Mater*. 2012;22:4763-4770.

doi: 10.1002/adfm.201200922

49. Muntaha ST, Syed JAS, Mateen M, *et al.* Polymeric carbon nitride-based semiconductors as a beneficial candidate in photocatalysis diversity: A comprehensive review. *Chem Eng J*. 2025;519:165004

doi: 10.1016/j.cej.2025.165004

50. She X, Xu H, Xu Y, *et al.* Exfoliated graphene-like carbon nitride in organic solvents: enhanced photocatalytic activity and highly selective and sensitive sensor for the detection of trace amounts of Cu^{2+}. *J Mater Chem A*. 2014;2:2563.

doi: 10.1039/c3ta13768f

51. Chen F, Wu C, Zheng G, *et al.* Few-layer carbon nitride photocatalysts for solar fuels and chemicals: Current status and prospects. *Chin J Catal*. 2022;43:1216-1229.

doi: 10.1016/s1872-2067(21)63985-2

52. Zhang X, Xie X, Wang H, *et al.* Enhanced photoresponsive ultrathin graphitic-phase C_3N_4 nanosheets for bioimaging. *J Am Chem Soc*. 2013;135:18-21.

doi: 10.1021/ja308249k

53. Coleman JN, Lotya M, O'Neill A, *et al.* Two-dimensional nanosheets produced by liquid exfoliation of layered materials. *Science*. 2011;331:568-571.

doi: 10.1126/science.1194975

54. Yang S, Gong Y, Zhang J, *et al.* Exfoliated graphitic carbon nitride nanosheets as efficient catalysts for hydrogen evolution under visible light. *Adv Mater*. 2013;25:2452-2456.

doi: 10.1002/adma.201204453

55. Han Q, Wang B, Gao J, *et al.* Atomically Thin Mesoporous Nanomesh of Graphitic C_3N_4 for High-Efficiency Photocatalytic Hydrogen Evolution. *ACS Nano*. 2016;10:2745-2751.

doi: 10.1021/acsnano.5b07831

56. Li Q, Zhang P, Hong T, *et al.* Highly-efficient photocatalytic removal of methyl orange on CuO hierarchical hollow microspheres modified by ultrathin and porous g-C_3N_4 nanosheets. *J Environ Manag*. 2025;381:125233.

doi: 10.1016/j.jenvman.2025.125233

57. Lü H, Wang D, Yang P, *et al.* WO_3 implanted Pt-g-C_3N_4 nanosheets towards boosted photocatalytic tetracycline hydrochloride removal and water splitting. *J Environ Chem Eng*. 2025;13:118685.

doi: 10.1016/j.jece.2025.118685

58. Ju Q, Hu Y, Liu Q, *et al.* Source apportionment and ecological health risks assessment from major ions, metalloids and trace elements in multi-aquifer groundwater near the Sunan mine area, Eastern China. *Sci Total Environ*. 2023;860:160454.

doi: 10.1016/j.scitotenv.2022.160454

59. Xing W, Chen G, Li C, *et al.* Construction of Large-Scale Ultrathin Graphitic Carbon Nitride Nanosheets by a Hydrogen-Bond-Assisted Strategy for Improved Photocatalytic Hydrogen Production and Ciprofloxacin Degradation Activity. *Chem Cat Chem*. 2016;8:2838-2845.

doi: 10.1002/cctc.201600397

60. Huang J, Zhong J, Yao R, *et al.* Enhanced peroxymonosulfate activation through visible-light-responsive ultrathin phosphorus-iron-codoped g-C_3N_4 nanosheets for efficient naproxen degradation. *J Colloid Interface Sci*. 2026;701:138667.

doi: 10.1016/j.jcis.2025.138667

61. Kalantari Bolaghi Z, Rodriguez-Seco C, Yurtsever A, *et al.* Exploring the Remarkably High Photocatalytic Efficiency of

Ultra-Thin Porous Graphitic Carbon Nitride Nanosheets. *Nanomaterials*. 2024;14:103.

doi: 10.3390/nano14010103

62. Xu J, Zhang L, Shi R, *et al.* Chemical exfoliation of graphitic carbon nitride for efficient heterogeneous photocatalysis. *J Mater Chem A*. 2013;1:14766.

doi: 10.1039/c3ta13188b

63. Wang M-m, Li Q-y, Liu J-g, *et al.* Facile synthesis of novel 2D mesoporous g-C_3N_4/TiO_2 heterojunction composites with high photocatalytic performance. *Ceram Int*. 2025;51:30948-30958.

doi: 10.1016/j.ceramint.2025.04.287

64. Liu S, Tang J, Yu X-f, *et al.* Engineering $CoOH_2$/mesoporous g-C_3N_4 composites for synergistic radical/non-radical antibiotic degradation via electron-bridged peroxymonosulfate activation. *J Environ Chem Eng*. 2025;13:118457.

doi: 10.1016/j.jece.2025.118457

65. Vinu A, Two-Dimensional Hexagonally-Ordered Mesoporous Carbon Nitrides with Tunable Pore Diameter, Surface Area and Nitrogen Content. *Adv Funct Mater*. 2008;18:816-827.

doi: 10.1002/adfm.200700783

66. Jin X, Balasubramanian VV, Selvan ST, *et al.* Highly ordered mesoporous carbon nitride nanoparticles with high nitrogen content: a metal-free basic catalyst. *Angew Chem Int Ed Engl.* 2009;48:7884-7887.

doi: 10.1002/anie.200903674

67. Zhang J, Guo F, Wang X. An Optimized and General Synthetic Strategy for Fabrication of Polymeric Carbon Nitride Nanoarchitectures. *Adv Funct Mater*. 2013;23:3008-3014.

doi: 10.1002/adfm.201203287

68. Ismael M, Shang Q, Yue J, Wark M. Photooxidation of biomass for sustainable chemicals and hydrogenproduction on graphitic carbon nitride-based materials: Acomprehensive review. *Mater Today Sustain*. 2024;27:100827.

doi: 10.1016/j.mtsust.2024.100827

69. Lakhi KS, Cha WS, Joseph S, *et al.* Cage type mesoporous carbon nitride with large mesopores for CO_2 capture. *Catal Today*. 2015;243:209-217.

doi: 10.1016/j.cattod.2014.08.036

70. Ruban SM, Singh G, Ramadass K, *et al.* Aminoguanidine Derived N-Rich Mesoporous Carbon Nitrides with Tunable Nitrogen Contents for Knoevenagel Condensation. *Chem Cat Chem*. 2023;15:e202300240

doi: 10.1002/cctc.202300240

71. Zheng Y, Hang Z, Ouyang J, *et al.* Hierarchical Design of 2D Carbon Nitride and Derivatives for Next-Generation Energy Conversion and Storage Technologies. *Small*. 2025;21:e05924.

doi: 10.1002/smll.202505924

72. Zhang X-W, Xu J-Y, Yu Z-H, *et al.* Mesostructured carbon nitride synthesized by NaOH-assisted detemplation for enhanced catalytic synthesis of dimethyl carbonate from ethylene carbonate. *Appl Catal A Gen*. 2025;693:120120.

doi: 10.1016/j.apcata.2025.120120

73. Ranganathan VRPA, Rao C. Hydrothermal Synthesis of Organic ChannelStructures: 1:1 Hydrogen-Bonded Adducts ofMelamine with Cyanuric and Trithiocyanuric Acids. *J Am Chem Soc*. 1999;121:1752-1753.

doi: 10.1021/ja983928o

74. Zhou B, Zhang C, Li Y, *et al.* General self-fission strategy via supramolecular self-assembly for high-yield and cost-effective synthesis of g-C_3N_4 nanostructures for photocatalytic hydrogen evolution. *J Colloid Interface Sci*. 2025; 695: 137787.

doi: 10.1016/j.jcis.2025.137787

75. Liang Q, Liu X, Shao B, *et al.* Construction of fish-scale tubular carbon nitride-based heterojunction with boosting charge separation in photocatalytic tetracycline degradation and H_2O_2 production. *Chem Eng J*. 2021;426:130831.

doi: 10.1016/j.cej.2021.130831

76. Zhang M, Zhang Y, Tang L, *et al.* Synergetic utilization of 3D materials merits and unidirectional electrons transfer of Schottky junction for optimizing optical absorption and charge kinetics. *Appl Catal B Environ*. 2021;295:120278.

doi: 10.1016/j.apcatb.2021.120278

77. Yang H, Sun S, Yang Q, *et al.* Emerging In-Plane Junctions in Graphitic Carbon Nitride for Remarkably Enhanced Photocatalysis. *Adv Funct Mater*. 2025;35:e10882.

doi: 10.1002/adfm.202510882

78. Hou G, Dong W, Li Z, *et al.* Donor-Acceptor characteristic g-C_3N_4 hollow nanospheres heterojunctions for efficient photocatalytic uranium reduction. *J Solid State Chem*. 2024;336:124739.

doi: 10.1016/j.jssc.2024.124739

79. Zheng Z, Wang X, Ye Z, *et al.* In situ growth $ZnIn_2S_4$ nanosheets on g-C_3N_4 nanorods with boosted charge transfer for high-efficient photocatalysis removal of U(VI). *Sep Purif Technol*. 2025;364:132271.

doi: 10.1016/j.seppur.2025.132271

80. Bai X, Wang L, Zong R, *et al.* Photocatalytic Activity Enhanced via g-C_3N_4 Nanoplates to Nanorods. *J Phys Chem C*. 2013;117:9952-9961.

doi: 10.1021/jp402062d

81. Zhang M, Zhang Y, Tang L, *et al.* Ultrathin Bi_2WO_6 nanosheets loaded g-C_3N_4 quantum dots: A direct Z-scheme photocatalyst with enhanced photocatalytic activity towards degradation of organic pollutants under wide spectrum light irradiation. *J Colloid Interface Sci*. 2019;539:654-664.

doi: 10.1016/j.jcis.2018.12.112

82. Li K, Li J, Qin F, *et al.* Nano zero valent iron in the 21st century: A data-driven visualization and analysis of research topics and trends. *J Clean Prod*. 2023;415:137812.

doi: 10.1016/j.jclepro.2023.137812

83. Li K, Tan H, Li J, *et al.* Unveiling the Effects of Carbon-Based Nanomaterials on Crop Growth: From Benefits to Detriments. *J Agric Food Chem*. 2023;71:11860-11874.

doi: 10.1021/acs.jafc.3c02768